GLIA

WILEY

RESEARCH ARTICLE

Homogeneity or heterogeneity, the paradox of neurovascular pericytes in the brain

Huimin Zhang | Xiao Zhang | Xiaoqi Hong | Xiaoping Tong

Center for Brain Science of Shanghai Children's Medical Center, Department of Anatomy and Physiology, Shanghai Jiao Tong University School of Medicine, Shanghai, China

Correspondence
Xiaoping Tong, Center for Brain Science of Shanghai Children's Medical Center, Department of Anatomy and Physiology, Shanghai Jiao Tong University School of Medicine, Shanghai, China.
Email: xtong@shsmu.edu.cn

Abstract

Pericytes are one of the main components of the neurovascular unit. They play a critical role in regulating blood flow, blood–brain barrier permeability, neuroinflammation, and neuronal activity. In the central nervous system (CNS), pericytes are classified into three subtypes, that is, ensheathing, mesh, and thin-strand pericytes, based on their distinct morphologies and region-specific distributions. However, whether these three types of pericytes exhibit heterogeneity or homogeneity with regard to membrane properties has been understudied to date. Here, we combined bulk RNA sequencing analysis with electrophysiological methods to demonstrate that the three subtypes of pericytes share similar electrical membrane properties in the CNS, suggesting a homogenous population of neurovascular pericytes in the brain. Furthermore, we identified an inwardly rectifying potassium channel subtype Kir4.1 functionally expressed in pericytes. Electrophysiological patch clamp recordings indicate that Kir4.1 channel currents in pericytes represent a small portion of the K^+ macroscopic currents in physiological conditions. However, a significant augmentation of Kir4.1 currents in pericytes was induced when the extracellular K^+ was elevated to pathological levels, suggesting pericytes Kir4.1 channels might play an important role as K^+ sensors and contribute to K^+ homeostasis in local neurovascular networks in pathology.

KEYWORDS
electrical membrane properties, Kir4.1 ion channels, neurovascular unit, pericyte, potassium sensor

1 | INTRODUCTION

Pericytes are mural cells with bump-on-a-log like morphology located on the outside of capillaries. They play important roles in maintaining blood–brain barrier integrity and providing microvascular basal tone (Berthiaume et al., 2018). More important, pericytes are ubiquitous in the capillary microcirculation of all vascular beds, reaching their highest densities within retinal and cerebral circulations and are integral components of the neurovascular unit (NVU), which ensures a prompt on-demand increase of local cerebral blood flow (CBF) in the brain (Verkhratsky et al., 2021). Different from the smooth muscle cells (SMCs), pericytes usually have much thinner processes that extend longitudinally along or around capillaries (Attwell et al., 2016). It is generally recognized that brain pericytes can be classified into

Huimin Zhang and Xiao Zhang contributed equally.

three subtypes: ensheathing, mesh and thin-strand pericytes (Gonzales & Klug, 2020; Grant et al., 2019). They can be distinguished in terms of their location and distinct morphologies. For instance, ensheathing pericytes are contractile cells that have short extensions and wrap around capillaries near the arteriole end of the capillary bed; mesh pericytes and thin-strand pericytes usually have much longer processes that lack α-SMA expression and are mostly located at capillaries further from the arteriole (Attwell et al., 2016; Gonzales & Klug, 2020; Grant et al., 2019; Kornfield & Newman, 2014). Thus, a heterogeneous characterization of pericytes has been based predominantly on cell structure, spatial distribution and diverse functions. Much less is known as to whether the three types of pericytes exhibit differences of intrinsic membrane properties. Therefore, distinguishing the phenotypic differences of brain pericytes still requires multiple identifications by using multiple methods such as endogenous transcriptomic/protein analysis and electrophysiological recordings of intrinsic properties.

Recently, studies have shown that vascular inwardly rectifying potassium channels (Kir) are the major extracellular potassium sensors in the control of CBF. Researchers found that high concentration of extracellular K^+ activates capillary endothelial cell Kir channels to produce a rapidly propagating retrograde hyperpolarization and sequentially causes an upstream arteriolar dilation by increasing blood flow into the capillary bed (Longden et al., 2017; Longden & Nelson, 2015). Kir channels have a general property that allows K^+ to flow inwardly when the resting membrane potential (RMP) is negative to the equilibrium potential for K^+ (E_K) (Hibino et al., 2010). This provides the driving force, mainly in glial cells, to uptake the K^+ released during neuronal activity and allow processing functions such as "K^+ spatial buffering". The specific expression of Kir4.1 subtype in astroglia has been well recognized for maintaining a hyperpolarized cell membrane potential and K^+ uptake in healthy and pathological conditions (Nwaobi et al., 2016; Olsen & Sontheimer, 2008; Tong et al., 2013, 2014; Zhang et al., 2018). In contrast, the functional role of Kir channels in pericytes remains poorly investigated. The major reason is due to the difficulty of accessing an individual pericyte around vascular capillaries in situ by classical electrophysiological patch-clamp methods, although previously a few studies have reported voltage-gated K^+ channels expressed in dissociated pericytes or capillaries in vitro (Cao et al., 2006; Liu et al., 2018; Matsushita & Puro, 2006).

Here, by using electrophysiological techniques and transcriptomic analysis, we characterized the intrinsic membrane properties of three subtypes of pericytes in the CNS. We further found that pericytes highly express *Kcnj10* gene-coding for Kir4.1 ion channels, which were thought mainly expressed in glial cells and largely contribute to cell membrane properties (Nwaobi et al., 2016; Song et al., 2018; Tong et al., 2014). In particular, pericyte Kir4.1 channels are more sensitive to the increase of extracellular potassium than astrocytic Kir4.1 channels, indicating Kir4.1 channel expressed in brain pericytes plays a crucial role as local K^+ sensor, thus mediating potassium homeostasis in the local neurovascular networks.

2 | MATERIALS AND METHODS

2.1 | Animals

All animal procedures complied with the animal care standards set forth by the US National Institutes of Health and were approved by the Institutional Animal Care and Use Committee (IACUC), Shanghai Jiao Tong University School of Medicine. All mice were kept on a C57BL/6 background and under a 12–12 hr light–dark cycle with food and water provided ad libitum from the cage lid. NG2DsRedBAC (Cspg4-DsRed.T1; JAX strain 008241| NG2DsRed) were obtained from The Jackson Laboratory (USA).

2.2 | Acute brain slice preparation

For the preparation of brain slices, 8-week-old mice were deeply anesthetized with 5% chloral hydrate and intracardially perfused with oxygenated ice-cold dissection buffer containing (in mM): 82.75 NaCl, 2.4 KCl, 6.8 MgCl$_2$, 0.5 CaCl$_2$, 1.4 NaH$_2$PO$_4$, 23.8 NaHCO$_3$, 23.7 D-glucose and 65 sucrose. Coronal hippocampal slices were cut at 300 μm thickness (VT1000S; Leica Microsystems, Germany) and allowed to equilibrate for at least 1 h at 31°C in aCSF containing (in mM): 125 NaCl, 2.5 KCl, 1 MgCl$_2$, 2 CaCl$_2$, 1.25 NaH$_2$PO$_4$, 25 NaHCO$_3$, and 12.5 D-glucose. All the buffers in this experiment were continuously bubbled with a mixture of 95% O$_2$/5% CO$_2$ gas.

2.3 | Electrophysiological recordings from acute brain slices

For brain slice whole-cell patch-clamp recordings, an individual slice was placed in the recording chamber and continuously perfused with oxygenated aCSF at room temperature. Slices were visualized with an upright epifluorescent microscope (BX51WI, Olympus, Tokyo, Japan) equipped with differential interference contrast optics and an infrared CCD camera (optiMOS, Q IMAGING, Olympus, Tokyo, Japan). All the electrophysiological recordings were made in hippocampal CA1 region with a MultiClamp 700B amplifier (Molecular Devices, Sunnyvale, CA). Signals were low-pass filtered at 2 kHz and sampled at 20 kHz using Digidata 1550A (Molecular Devices) and data were collected 2 min after obtaining a stable whole-cell configuration. Patch pipettes were pulled from borosilicate glass capillaries with a microelectrode puller (Model P-1000, Sutter Instruments).

For pericytes patch recordings, hippocampal slices (300 μm thick) were prepared from 8-week-old transgenic mice which express DsRed on pericytes under the control of *Cspg4* promoter. Glass pipettes with a resistance of 6–8 MΩ were filled with a low chloride intracellular solution containing (in mM): 125 K-gluconate, 15 KCl, 8 NaCl, 10 HEPES, 0.2 EGTA, 3 Na$_2$-ATP, 0.3 Na-GTP (pH to 7.3) and 20 μM Alexa-488 (Thermo Fisher, A10436, USA). In particular, brain slices were gently digested with papain for 10 min to dissociate the fascia wrapped on the pericyte before whole-cell patch recordings.

Moderate digestion can not only dissociate the fascia wrapped on the pericyte, but also keep the intact anatomical structure of the brain slice and the cells' viability.

2.4 | Induction of hypoxia in brain slices

Hypoxia was induced following a method described previously (Chao et al., 2007; Shankar & Quastel, 1972). In brief, hypoxia was obtained by switching the perfusion buffer from oxygen-gassed solution to a hypoxia solution (same composition) gassed with a mixture of 95% N_2/5% CO_2. The inward potassium currents of pericytes were obtained in acute hypoxic condition after the cells were recorded in oxygen-gassed solution as control.

2.5 | Immunohistochemistry and image analysis

For mouse immunohistochemistry, animals were anesthetized and perfused through the ascending aorta with a solution of normal saline for ∼3 min, followed by 4% paraformaldehyde in 0.1 M PB for 5 min. Brains were removed and post-fixed in 4% paraformaldehyde at 4°C overnight and then cut into 30-μm-thick coronal sections including cortex and hippocampus. These free-floating sections were incubated in permeabilizing buffer (0.3% Triton X-100 in PBS) for 15 min and then blocked with donkey serum (Ruite Biotechnology, w9030-05) (10% in PBS-T: PBS with 0.1% TritonX-100) for 2 h at room temperature. After that, sections were incubated overnight at 4°C with primary antibodies described below. Sections were washed with PBS-T three times for 15 min each and then placed in blocking solution containing secondary antibodies for 2 h at room temperature. For nuclei staining, sections were incubated with 4′,6′-diamidino-2-phenylindole dihydrochloride (DAPI, 1:1500, Cell Signaling 4083S) for 15 min.

The primary antibodies included goat antibody to Pdgfrβ (1:500; R&D system AF1042), GFAP (1:2000; Abcam ab7260). The corresponding secondary antibody is donkey anti-goat IgG 488 (1:500; Invitrogen, A11055) and donkey anti-rabbit IgG 568 (1:500; Invitrogen A10042). Sections were incubated with DAPI (1:1500; Cell Signaling) for 15 min at room temperature to label nuclei and mounted on glass slides in Fluoromount Aqueous Mounting Medium (AQUA-MOUNT, REF 13800). Slice images were acquired on a Leica TCS SP8 confocal microscope with HC PL APO CS2 × 20/air, ×40/oil objective and ×60/oil objective. The images of different channels were thresholded and image analysis was performed by Image-Pro Plus (Media Cybernetics).

2.6 | Single-cell RT-PCR and RNA-sequencing

Single pericytes with DsRed fluorescence labeling from NG2-DsRed mice at postnatal 8 weeks were selected and aspirated into a glass pipette from hippocampal acute slices following a method described previously with slight changes (Picelli et al., 2014; Toledo-Rodriguez & Markram, 2014). In brief, cells were picked promptly by micromanipulation and immediately placed in lysis buffer. To minimize the changes in gene expression and meet the quality requirement for cDNA used to construct sequencing libraries, three types of DsRed-positive cells were collected within 3 h after slice preparation. The selected pericytes were processed for single-cell RNA extraction and reverse transcription within 1 h and were subjected to cDNA amplification and purification. Single-cell cDNA was amplified using KAPA HiFi HotStart ReadyMix (2×; KAPA Biosystems, Cat. No. KK2601) according to the manufacturer's protocol. The RNA primers were generated using the following primers:

Kir4.1, Forward primer: CTGCCCCGCGATTTATCAGA;
Reverse primer: CATTCTCACATTGCTCCGGC.
GAPDH, Forward primer: GGCAAATTCAACGGCACAGT;
Reverse primer: TAGGGCCTCTCTTGCTCAGT.
DsRed, Forward primer: CCGACATCCCCGACTACAAG;
Reverse primer: TAGTCCTCGTTGTGGGAGGT.

For RNA-seq transcriptome experiment, 8-week-old NG2-DsRed mouse was anesthetized with isoflurane and the brain was removed. The fresh brain tissue was cut into small pieces and the minced tissue was incubated in 15 unit ml^{-1} papain at 31°C for 45 min. The digestion was stopped by protease inhibitor solution (Ovomucoid) (Zhang et al., 2016), after which, the tissue was immediately triturated and the isolated cells were seeded on coverslips. Single DsRed-labeled pericytes were selected and aspirated into a glass pipette. The total RNA of a pericyte in lysis buffer was converted to cDNA using the Smart-seq2 protocol and the cDNA was preamplified as described previously (Li et al., 2016; Picelli et al., 2014). Illumina libraries were prepared using the commercially Sample Preparation kit (Nextera XT DNA Library Prep Kit) according to the manufacturer's instructions. The single-cell Illumina libraries of each experiment were pooled and sequenced for 2 × 75-base Paired-End reads on Illumina NextSeq500 sequencing system at the Sequencing Core of Shanghai Institute of Immunology, Shanghai Jiao Tong University School of Medicine. Sequencing reads were inspected by Fastqc 0.11.3 to check the reads' quality and then aligned to the GRCm38/mm10 assembly of the mouse genome using Tophat 2.1.0 with the default options. FPKM (fragments per kilobase of exon per million fragments) values of each gene were obtained by Cufflinks 2.2.1 using genome annotation from UCSC (University of California, Santa Cruz). The GTF (gene transfer format) file was modified to update the genes encoding all inwardly rectifying potassium channel family members to the latest version archived in NCBI.

2.7 | Quantification and statistical analysis

All statistical tests were run in GraphPad InStat 3. The graphs were created in Origin 8 and assembled in CorelDraw 12. Data are presented as mean ± SEM. For each set of data to be compared, we determined in GraphPad Instat whether the data were normally distributed or not. If they were normally distributed we used parametric tests, as listed in the text. If the data were not normally distributed we used non-parametric tests, as indicated in the text. Paired and unpaired

Student's two tailed *t*-tests (as appropriate and as indicated in the text), parametric ANOVA with Tukey–Kramer multiple comparisons tests were used for most statistical analyses. For electrophysiological experiments, n values represent the number of recorded cells. For immunohistochemistry, n values represent the number of mice. No statistical methods were used to pre-determine sample size, or to randomize. Statistical significance was set at $*p < .05$, $**p < .01$, $***p < .001$.

2.8 | Chemicals and drug application

All chemicals for electrophysiology were purchased from Sigma-Aldrich. The potassium blocker barium chloride was dissolved in double-distilled water at 50 mM and stored in aliquots at $-20°C$. The blocker was bath applied at 100 μM working concentration. Kir4.1 channel antagonist VU0134992 was purchased from Med-ChemExpress and the working concentration was 15 μM. Kir6.1 channel bloker glibenclamide was purchased from Alomone lab and the working concentration was 10 μM.

2.9 | Data availability

The authors declare that all data supporting the findings of this study are available within the article and its supplementary information files. All relevant data not present within the manuscript are available from the corresponding author upon reasonable request. RNA-sequencing data are deposited at the Sequence Read Archive with SRA accession number PRJNA695351.

3 | RESULTS

3.1 | Specific labeling of vascular pericytes in NG2DsRedBAC transgenic mice

Neural/glial antigen 2 (NG2) is broadly expressed both in vascular pericytes and oligodendrocyte precursor cells (OPCs) (Birbrair, 2018; Zhu et al., 2008). We imaged pericytes by using transgenic reporter mice expressing DsRed (Discosoma red fluorescent protein) under the control of chondroitin sulfate proteoglycan 4 (*Cspg4*, *Ng2*) promoters which have been widely used in previous studies (Gonzales & Klug, 2020; Hall et al., 2014; Zhao et al., 2018). Since NG2 proteoglycan also express in OPCs, we first investigated pericyte specificity labeling by DsRed in NG2DsRedBAC transgenic mice during brain development. As platelet-derived growth factor receptor-β (Pdgfrβ) is another specific marker for putative pericytes (Cheng et al., 2018), we examined the colocalization rate of NG2-DsRed with Pdgfrβ in mouse hippocampus at postnatal 2, 4, 6, and 8 weeks, respectively. Immunohistochemistry showed that the colocalization rate of NG2-DsRed with Pdgfrβ was: 43.31% ± 3.21 at postnatal 2 weeks ($n = 3$ mice), 75.88% ± 10.11 at postnatal 4 weeks ($n = 4$ mice), 91.55% ± 0.68 at postnatal 6 weeks ($n = 3$ mice) and 99.45% ± 0.55 at postnatal

8 weeks ($n = 4$ mice), respectively (Figure 1a–c). As DsRed labeled most pericytes in the hippocampus with increasing age in NG2DsRedBAC mouse strain, we therefore set 8-week-old NG2DsRedBAC mice for all following experiments in the study.

3.2 | Identification of intrinsic membrane properties of three subtypes of pericytes

To identify the intrinsic membrane properties of the three subtypes of pericytes, we used whole-cell patch clamp recordings to measure the RMP, membrane input resistance, and macroscopic currents of each individual pericyte in situ using an improved electrophysiological technique (also see the methods section for more details). As astrocyte end-feet usually overlay pericytes in the capillaries (Giannoni et al., 2018), we combined electrophysiological and histological methods to first identify the morphology of the patched cell by injection of Alexa Fluor 488 in the patch pipette while performing whole-cell patch clamp recordings. An intact cell morphology of fluorescent labeled pericyte can thus be imaged after acute brain slice post-fixation. Based on the distinct morphology and location of recorded pericytes, we found that thin-strand pericytes had long thin processes extending along a blood vessel and distributed in the brain broadly (Figure 2a). The average RMP was $-59.57 ± 3.74$ mV (Figure 2b, $n = 7$ cells). The average cell membrane input resistance was 308.25 ± 62.23 MΩ (Figure 2c, $n = 5$ cells). As shown in Figure 2d,e, thin-strand pericytes exhibited voltage-dependent K^+ macroscopic currents. At the command voltage of -142 and $+48$ mV, the average K^+ currents in thin-strand pericytes were $-372.03 ± 66.13$ pA and 497.96 ± 68.33 pA (Figure 2d,e, $n = 7$ cells), respectively. For mesh pericytes, mainly located on the proximal side of a capillary with a higher coverage area than thin-strand pericytes and adopting a mesh-like appearance (Figure 2a). The average RMP was $-59.15 ± 2.43$ mV (Figure 2b, $n = 7$ cells) and the average cell membrane input resistance was 222 ± 6.69 MΩ (Figure 2c, $n = 5$ cells). At the command voltage of -142 and $+48$ mV, the average K^+ currents in mesh pericytes were $-433.32 ± 43.25$ pA and 582.97 ± 63.28 pA, respectively (Figure 2d,e, $n = 8$ cells). The third subtype, ensheathing pericytes were positioned at the transitions between arterioles and capillaries (Figure 2a). Ensheathing pericytes shared similar electrical membrane properties with the other two subtypes of pericytes. The average RMP was $-57.86 ± 4.11$ mV (Figure 2b, $n = 7$ cells) and the average cell membrane input resistance was 214.76 ± 38.26 MΩ (Figure 2c, $n = 5$ cells). At the command voltage of -142 and $+48$ mV, the average K^+ currents in ensheathing pericytes were $-505.11 ± 126$ pA and 651.40 ± 137.52 pA, respectively (Figure 2d,e, $n = 5$ cells). Although pericytes have been classified into three distinct subtypes, we were surprised to find that there were no differences of the intrinsic membrane properties, i.e., membrane input resistance and RMP among different subtypes (Figure 2b–e, $p > .05$, ANOVA Tukey–Kramer multiple comparisons), suggesting a homogenous population of all three types of neurovascular pericytes in the adult brain, at least in terms of electrophysiological properties.
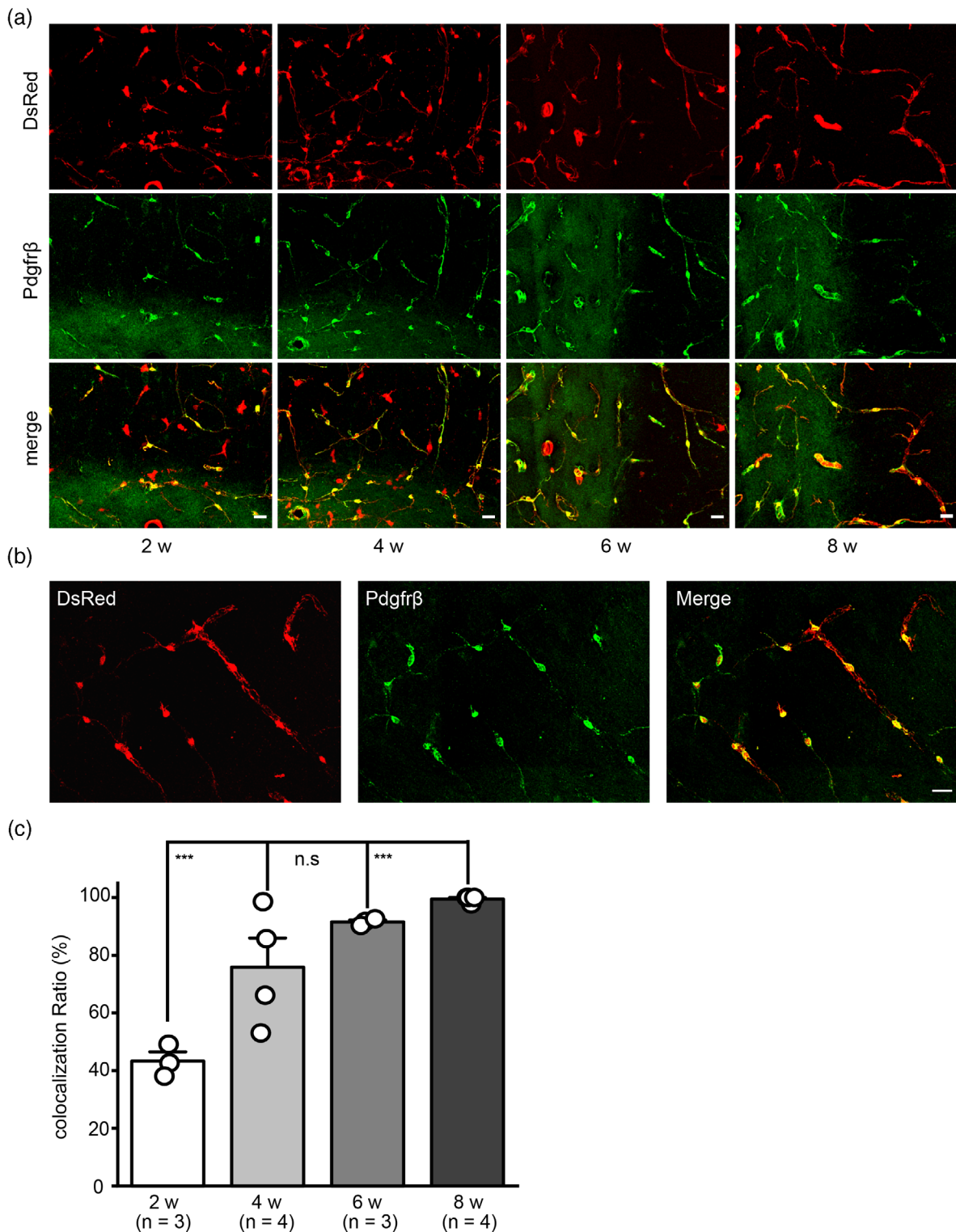
FIGURE 1 Specific labeling of pericytes in NG2DsRedBAC transgenic mice hippocampus during brain development. (a) Representative images showing the colocalization (in yellow) between DsRed (in red) and Pdgfrβ (in green) in NG2-DsRed mouse hippocampus at postnatal 8 weeks. Scale bars, 20 μm. (b) Representative images at high resolution showing the colocalization (in yellow) between DsRed (in red) and Pdgfrβ (in green) at 8-week NG2-DsRed mouse hippocampus. Scale bar, 20 μm. (c) Summary bar graph shows the colocalization ratio between DsRed and Pdgfrβ in NG2-DsRed mice hippocampus at different developmental stages. 2-week-old group: 43.31% ± 3.21, $n = 3$ mice; 4-week-old group: 75.88% ± 10.11, $n = 4$ mice; 6-week-old group: 91.55% ± 0.68, $n = 3$ mice; 8-week-old group: 99.45% ± 0.55, $n = 4$ mice. The error bars represent SEM, two-tailed unpaired *T*-test, *p* values are indicated as compared with postnatal 8-week-old group as control. n.s indicates not significant
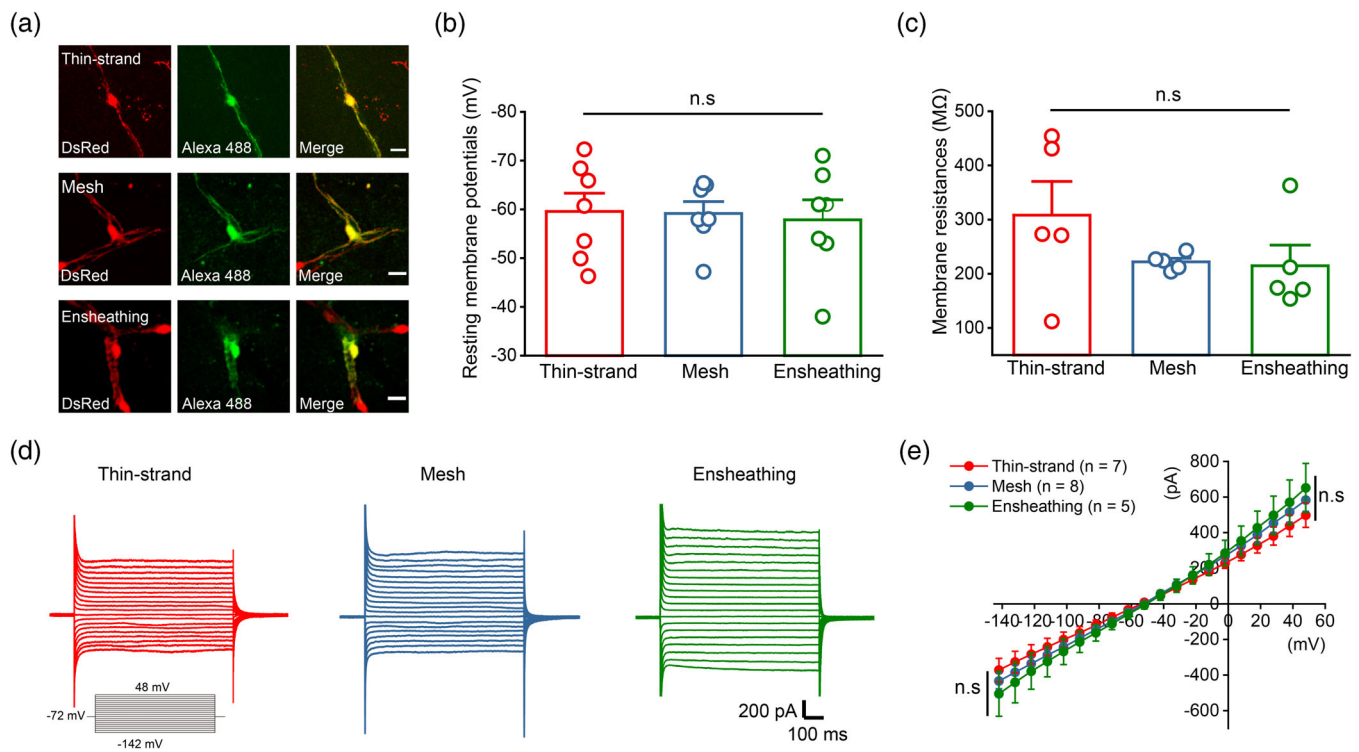
FIGURE 2 Characterization of electrical membrane properties of the three subtypes of pericytes. (a) Representative images showing the distinct morphology of three subtypes of post-fixed pericytes loaded with Alexa Fluor 488 in NG2DsRedBAC mouse hippocampus. The colocalization between DsRed (in red) and Alexa 488 (in green) is shown in yellow. Scale bars, 10 μm. (b) Bar graph summary showing the resting membrane potentials of three subtypes of pericytes. $n = 7$ cells for each group. The error bars represent SEM ANOVA Tukey–Kramer multiple comparisons, n.s indicates not significant. (c) Bar graph summary showing the membrane resistances of three subtypes of pericytes. $n = 5$ cells for each group. The error bars represent SEM ANOVA Tukey–Kramer multiple comparisons, n.s indicates not significant. (d) Representative traces show the voltage-dependent macroscopic currents from thin-strand (in red, $n = 7$ cells), mesh (in blue, $n = 8$ cells) and ensheathing (in green, $n = 5$ cells) pericytes. (e) Summary graph shows the average I/V plot of three subtypes of pericytes as indicated in (d). There is no significant difference of macroscopic K^+ currents among the three subtypes of pericytes

3.3 | Transcriptomic characterization of Kir mRNA expression in pericytes

It is well known that the NVU demands the rapid coupling of neuronal activity to blood flow responses. One factor that fits this profile is external potassium ions. Although the Kir channels expressed in astrocytic endfeet, which wrap the entirety of the parenchymal vasculature, are well studied in the dynamic regulation of local CBF (Longden & Nelson, 2015), increased evidence has shown that pericytes express functional inwardly rectifying potassium channels (Cao et al., 2006; Matsushita & Puro, 2006) and strongly suggest a potential role of Kir channel activation in the control of blood flow in the vascular wall mediated by external K^+ (Longden et al., 2017; Sonkusare et al., 2016). However, the expression of Kir isoforms in brain pericytes are still unclarified. Our initial results indicated that the three subtypes of pericytes share similar intrinsic membrane properties and voltage-dependent macroscopic K^+ channel currents (Figure 2). This prompted us to further investigate the subtype of Kir channel which contributes to the electrophysiological membrane properties of pericytes. Combining RNA-seq transcriptome analysis and single-cell reverse transcriptase polymerase chain reaction (RT-PCR) technique in NG2-DsRed transgenic mouse brain (Figure 3a–d), we indeed found that

abundant genes of inwardly rectifying K^+ channel subunits expressed in sorted pericytes as shown in Figure 3b. In particular, the top three seeded Kir channel genes were *Kcnj8*, *Kcnj10*, and *Kcnj9* among Kir channel genes family. Notably, the heat map and the pie chart showed a secondary enrichment of *Kcnj10*-coded Kir4.1 channel expressed in pericytes in NG2-DsRed transgenic mice (Figure 3b, $n = 4$ mice). Moreover, single-cell RT-PCR clearly demonstrated that Kir4.1 mRNA ubiquitously expressed in the three subtypes of DsRed labeled pericytes in situ (Figure 3c,d). In summary, our results are consistent with a previous study which found *kcnj8*-coded Kir6.1 abundantly expressed in brain pericytes by using in situ hybridization (Bondjers et al., 2006). However, we unexpectedly found that *Kcnj10* mRNA also expressed in vascular pericytes, which was thought to be expressed exclusively in glial cells in the CNS (Nwaobi et al., 2016).

3.4 | Elevation of external K^+ activates Kir4.1 channels in pericytes

To gain further insights into the role of Kir4.1 ion channels in pericytes, we measured current/voltage (I/V) relations before and during
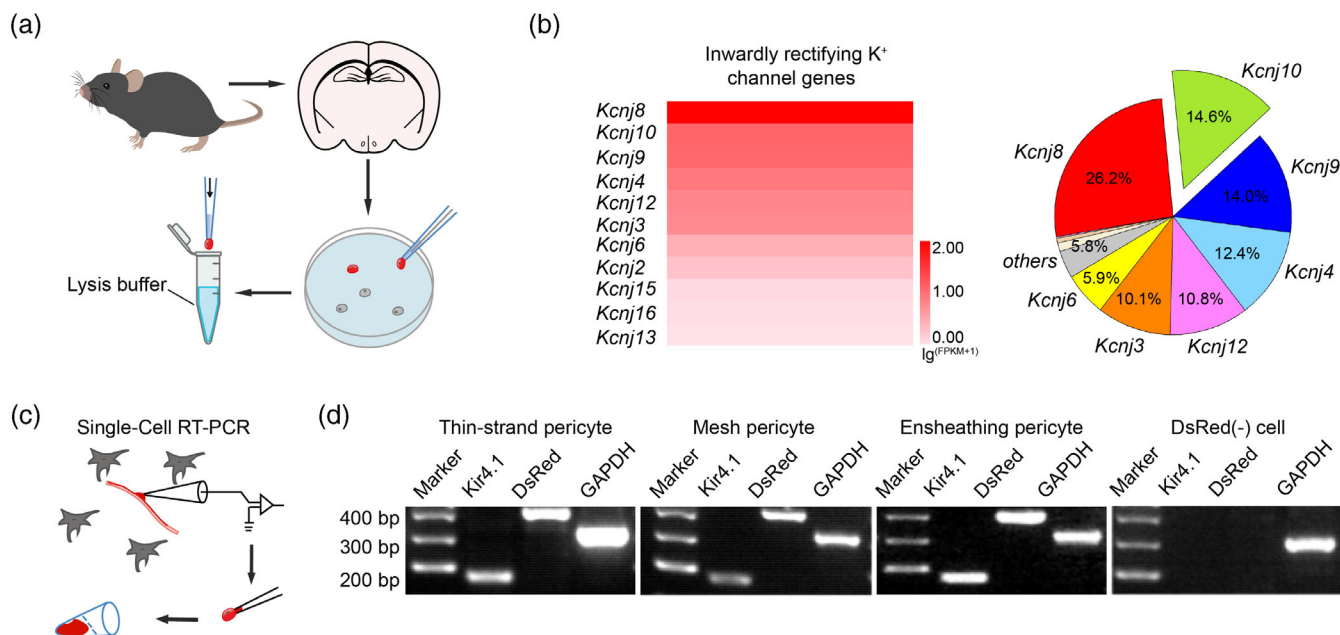
FIGURE 3 Bulk RNA sequencing analysis and single-cell RT-PCR in 8-week-old NG2-DsRed transgenic mice. (a) Experimental diagram showing the approach for DsRed-labeled pericyte collection from a 8-week-old NG2-DsRed transgenic mouse hippocampus by patch clamp method. (b) The heat map shows the abundance of mRNA (based on $lg^{(FPKM + 1)}$) for inwardly rectifying K^+ channel subunits expressed in pericytes. The FPKM value of each inwardly rectifying K^+ channel subunits gene is: *Kcnj8*: 159.00; *Kcnj10*: 15.90; *Kcnj9*: 14.26; *Kcnj4*: 10.01; *Kcnj12*: 7.07; *Kcnj3*: 6.08; *Kcnj6*: 2.14; *Kcnj2*: 1.08; *Kcnj15*: 0.25; *Kcnj16*: 0.13; *Kcnj13*: 0.041. The pie chart shows the proportion of each inwardly rectifying K^+ channel gene expressed in pericytes based on the results of RNA-seq transcriptome analysis, $n = 4$ mice. Notably, high level of *kcnj10* mRNA expression was found in DsRed-labeled pericytes. (c) Experimental diagram showing the approach for RNA isolation from single pericytes in situ. Each subtype of pericyte is identified by performing whole-cell patch-clamp recordings and the DsRed fluorescent expression at their region-specific distribution along the blood vessels. (d) At the end of recordings, the pericyte's cytoplasm is extracted by using glass pipettes for subsequent RT-PCR. Representative images show that thin-strand, mesh and ensheathing pericytes are positive for both DsRed and Kir4.1 mRNA expression, whereas a DsRed negative cell does not express Kir4.1 mRNA. $n = 3$ cells for each subtype of pericytes. Amplicon size for each mRNA: Kir4.1: 168 bp, DsRed: 394 bp, GAPDH: 317 bp

application of the Kir4.1 channel blocker barium chloride (100 μM), which was used to isolate K^+ channel currents mediated by Kir4.1 ion channels in glial cells, as previously described (Cui et al., 2018; Song et al., 2018; Tong et al., 2014). Interestingly, we found that there was barely detectable Ba^{2+}-sensitive Kir4.1 currents in vascular pericytes when external K^+ concentration was held at a physiological level, that is, 2.5 mM. The percentage of Kir4.1 currents of total K^+ macroscopic currents in pericytes was 1.13% ± 1.99 ($n = 12$ cells) compared with 33.04% ± 3.82 ($n = 11$ cells) in astrocytes under 2.5 mM $[K^+]_o$ when cell voltage was held at −142 mV (Figures 4a,b,g,h and 5c,d,g,h). The reason was possibly due to the closed state of Kir4.1 ion channels in pericytes under physiological conditions and could explain why the resting membrane potential of pericytes was relatively depolarized.

It is well known that active neurons release K^+ during the repolarization phase of the action potential and sequentially cause incremental increases in local K^+ concentration in the brain's external milieu. Furthermore, under pathological conditions such as seizure or ischemia, $[K^+]_o$ can rise substantially higher to 12–70 mM (Chao et al., 2007; Milton & Smith, 2018; Moody et al., 1974; Syková et al., 1994). To examine whether the open probability of Kir4.1 channels in pericytes increases under a fluctuation of external K^+, we next assessed Ba^{2+}-sensitive Kir4.1

currents in pericytes under 15 and 50 mM $[K^+]_o$, respectively. Indeed, when the cell's voltage was held at −142 mV, the average of Kir4.1 currents for basal condition was −0.048 ± 4.56 pA ($n = 12$ cells), −103.42 ± 16.94 pA for 15 mM $[K^+]_o$ ($n = 7$ cells) and − 214.41 ± 32.72 pA for 50 mM $[K^+]_o$ ($n = 11$ cells) ($p < .001$, two-tailed unpaired T-test, Figure 4a–g). The percentage of Kir4.1 channel currents from the total macroscopic K^+ currents was increased to 21% and 35% in pericytes by 15 mM $[K^+]_o$ and 50 mM $[K^+]_o$ when the cell's voltage was held at −142 mV (1.13% ± 1.99 for basal, 21.86% ± 3.78 for 15 mM $[K^+]_o$ and 34.75% ± 3.25 for 50 mM $[K^+]_o$, $n = 12, 7$ and 11 cells for basal, 15 mM $[K^+]_o$ and 50 mM $[K^+]_o$ group, respectively, $p < 0.001$, two-tailed unpaired T-test, Figure 4h), indicating that high K^+ concentration has a robust opening effect on Kir4.1 ion channels and the elevation of $[K^+]_o$ induces a dose-dependent increase of pericyte Kir4.1 channel currents in pericytes. In summary, we found that although Ba^{2+}-sensitive Kir4.1 currents in pericytes represent a very small portion of the K^+ macroscopic currents (1.13% of the total K^+ currents at the holding voltage of −142 mV) at a physiological $[K^+]_o$ level, surprisingly, these pericyte Kir4.1 channels are strongly activated by the elevation of the external K^+ to a pathological level at high concentrations such as 15 or 50 mM.
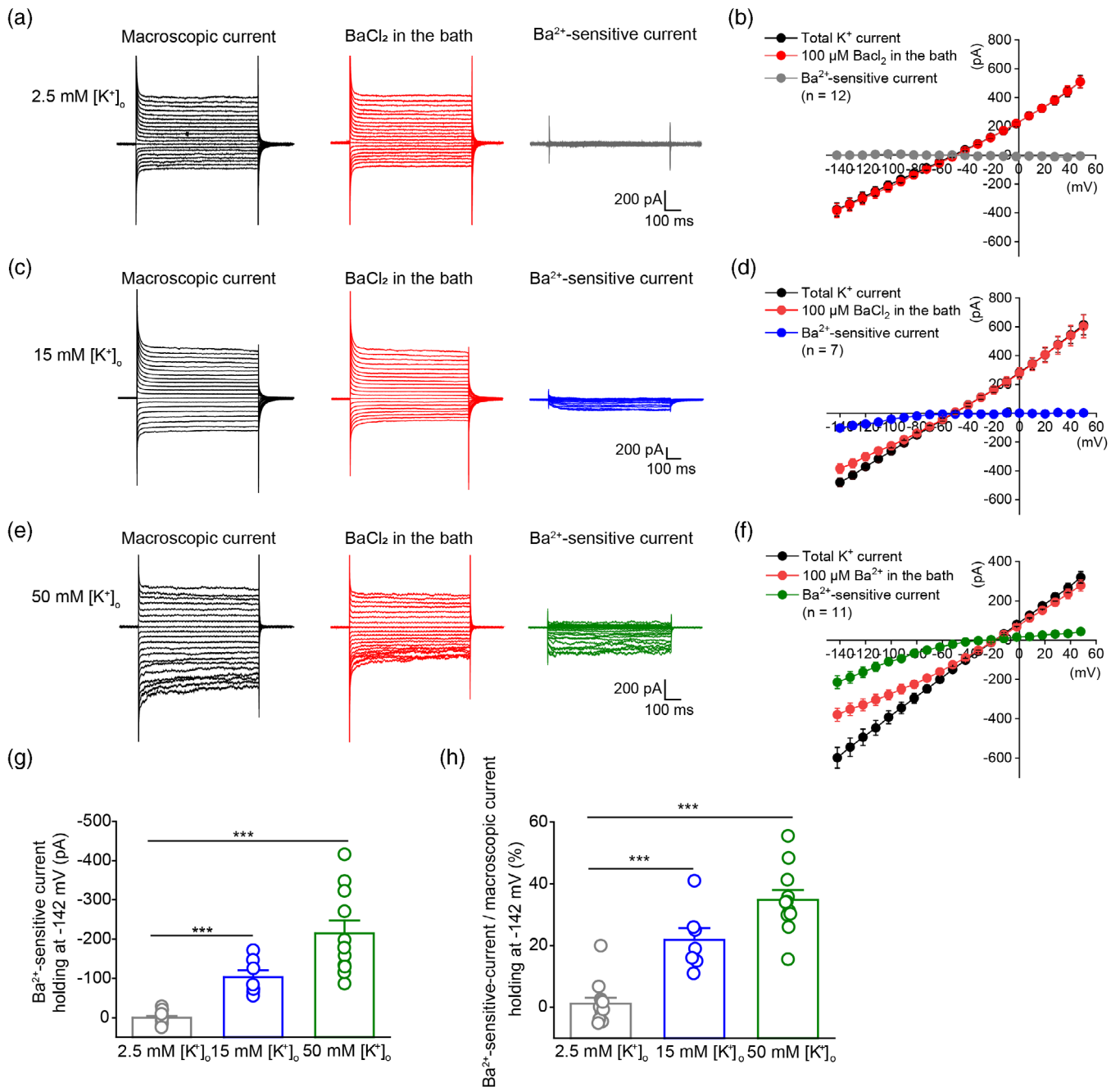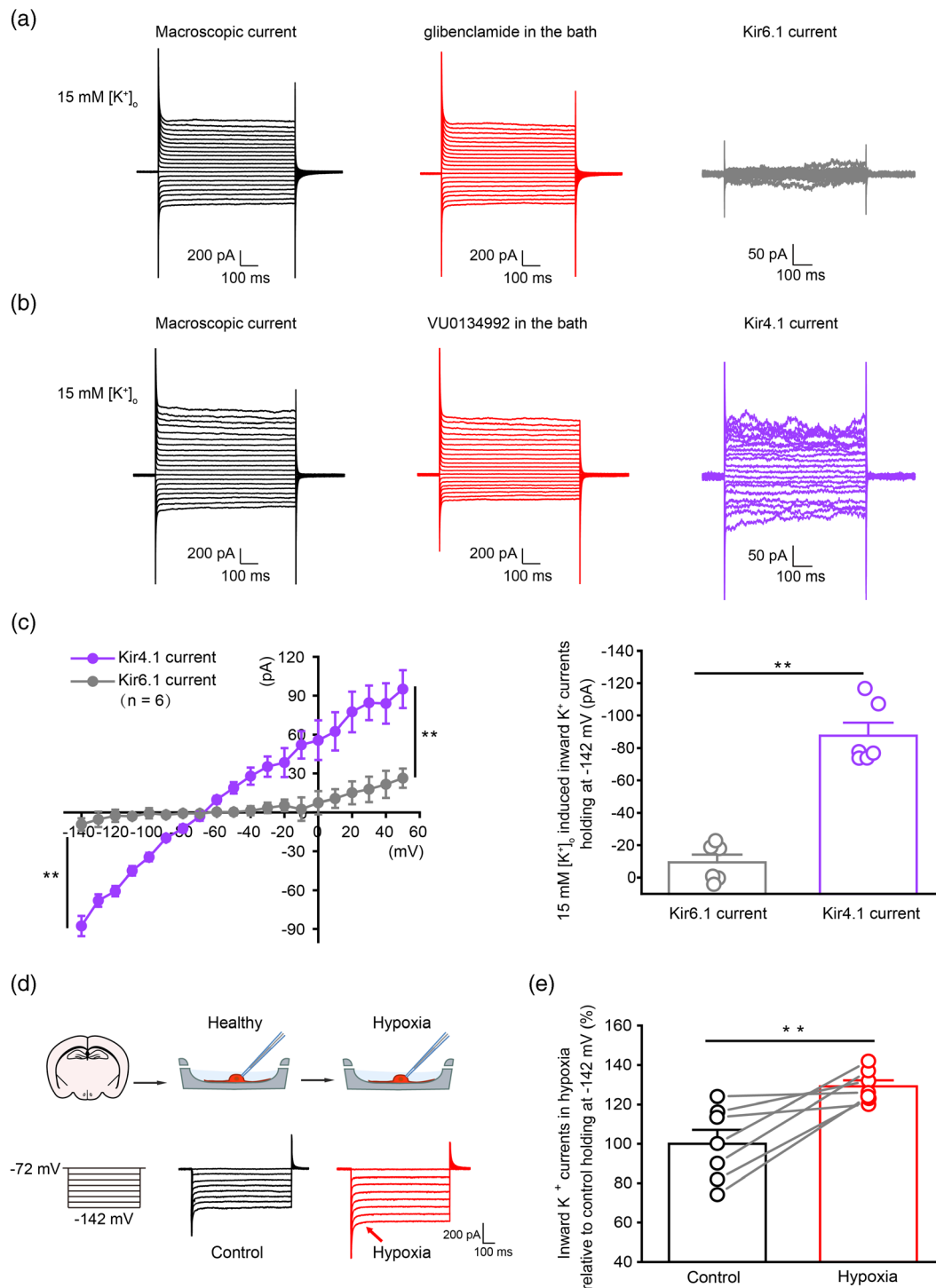
FIGURE 4 Elevation of external K$^+$ activates Kir4.1 channels in pericytes. (a) Representative traces show macroscopic K$^+$ currents (in black), macroscopic currents after bath application of Ba^{2+} (in red) and Ba^{2+}-sensitive currents (in gray) in a whole-cell patched pericyte in NG2-DsRed transgenic mouse hippocampus. (b) Average I/V plot shows there is no detectable Ba^{2+}-sensitive currents in pericytes under normal conditions at 2.5 mM [K$^+$]$_o$. The error bars represent SEM, $n = 12$ cells. (c) Representative traces show macroscopic K$^+$ currents in 15 mM [K$^+$]$_o$ (in black), macroscopic currents after bath application of Ba^{2+} in 15 mM [K$^+$]$_o$ (in red) and Ba^{2+}-sensitive currents in 15 mM [K$^+$]$_o$ (in blue) in a whole-cell patched pericyte in NG2-DsRed transgenic mouse hippocampus. (d) Average I/V plot shows the macroscopic and Ba^{2+}-sensitive currents in 15 mM [K$^+$]$_o$. The error bars represent SEM, $n = 7$ cells. (e) Representative traces show macroscopic K$^+$ currents in 50 mM [K$^+$]$_o$ (in black), macroscopic currents after bath application of Ba^{2+} in 50 mM [K$^+$]$_o$ (in red) and Ba^{2+}-sensitive currents in 15 mM [K$^+$]$_o$ (in green) in a whole-cell patched pericyte in NG2-DsRed transgenic mouse hippocampus. (f) Average I/V plot shows the macroscopic and Ba^{2+}-sensitive currents in 50 mM [K$^+$]$_o$. the error bars represent SEM $n = 11$ cells. (g) Bar graph summary shows the augmentation in Ba^{2+}-sensitive currents under 2.5 mM [K$^+$]$_o$ (in gray), 15 mM [K$^+$]$_o$ (in blue) and 50 mM [K$^+$]$_o$ (in green) when the cell's voltage was held at -142 mV. N $= 12$, 7 and 11 cells for 2.5, 15, and 50 mM [K$^+$]$_o$ group, respectively. *** indicates $p < .001$, two-tailed unpaired T-test. (h) Bar graph summary shows the percentage of Ba^{2+}-sensitive currents from the total macroscopic currents under 2.5 mM [K$^+$]$_o$ (in gray), 15 mM [K$^+$]$_o$ (in blue), and 50 mM [K$^+$]$_o$ (in green) when the cell's voltage was held at -142 mV. $n = 12$, 7, and 11 cells for 2.5, 15, and 50 mM [K$^+$]$_o$ group, respectively. The error bars represent SEM. *** indicates $p < .001$, two-tailed unpaired T-test
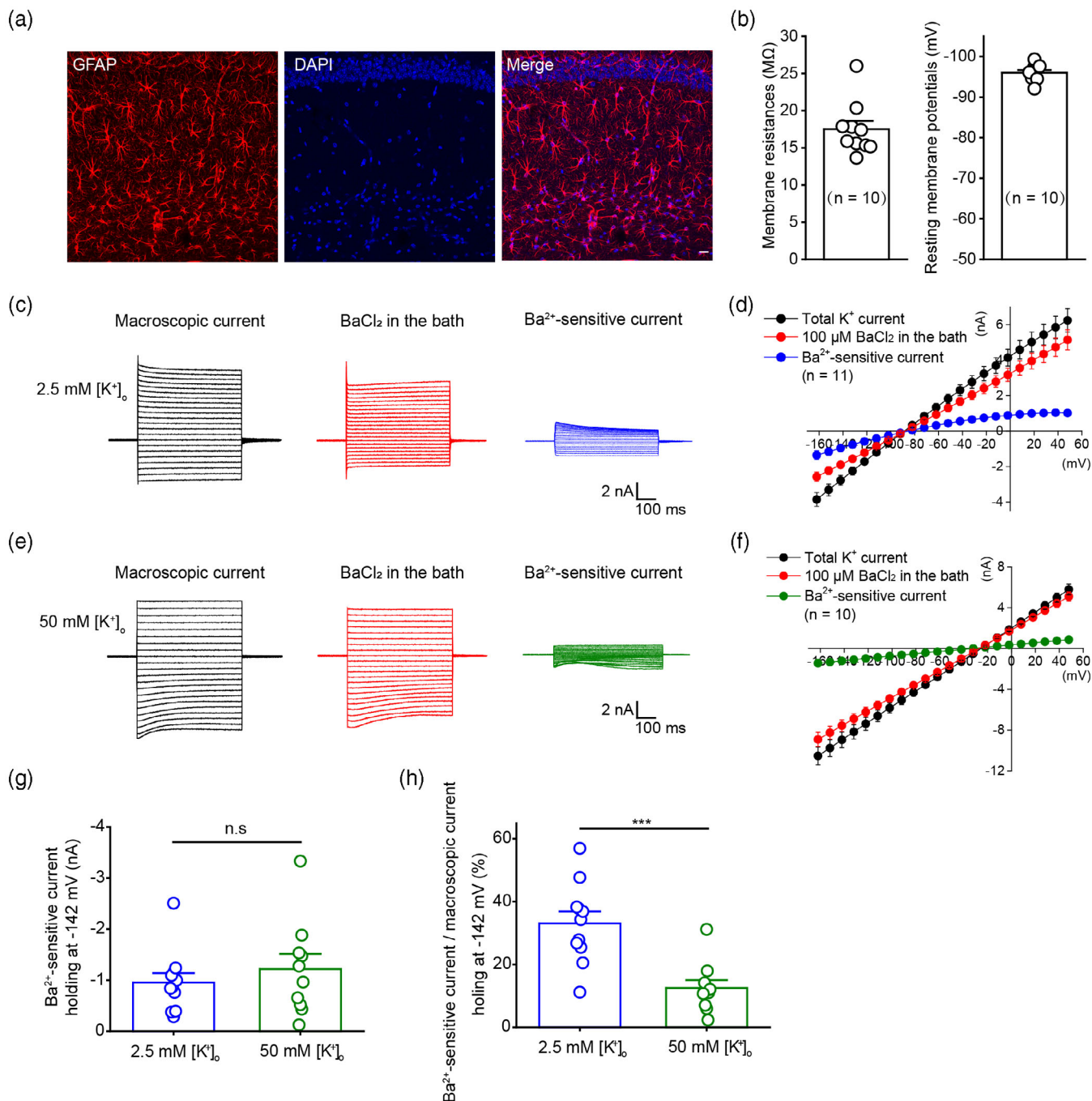
FIGURE 5 Astrocytic Kir4.1 channel currents do not change under 2.5 mM $[K^+]_o$ and 50 mM $[K^+]_o$. (a) Representative images show that a large number of GFAP-labeled astrocytes evenly distribute in the CA1 region of wild-type mouse hippocampus. (b) Bar graphs summary show the RMPs and membrane input resistances of astrocytes. $n = 10$ cells recorded. The error bars represent SEM. (c) Representative traces show macroscopic K^+ currents (in black), macroscopic currents after bath application of Ba^{2+} (in red) and Ba^{2+}-sensitive Kir4.1 currents (in blue) in a whole-cell patched astrocyte under 2.5 mM $[K^+]_o$ in wild-type mouse hippocampus. (d) Average I/V plot shows the Ba^{2+}-sensitive Kir4.1 currents in astrocytes in 2.5 mM $[K^+]_o$. $n = 11$ cells. (e) Representative traces show macroscopic K^+ currents (in black), macroscopic currents after bath application of Ba^{2+} (in red) and Ba^{2+}-sensitive Kir4.1 currents (in green) in a whole-cell patched astrocyte under 50 mM $[K^+]_o$ in wild-type mouse hippocampus. (f) Average I/V plot shows the macroscopic K^+ currents and Ba^{2+}-sensitive Kir4.1 currents in 50 mM $[K^+]_o$. $n = 10$ cells. (g) Bar graph summary shows the Ba^{2+}-sensitive Kir4.1 currents in 2.5 mM $[K^+]_o$ (in blue) and 50 mM $[K^+]_o$ (in green) when the cell's voltage was held at -142 mV. $n = 11$ and 10 cells for 2.5 and 50 mM $[K^+]_o$ group, respectively. n.s indicates not significant, two-tailed unpaired *T*-test. (h) Bar graph summary shows a decrease of the percentage of Ba^{2+}-sensitive Kir4.1 currents among total macroscopic K^+ currents in 50 mM $[K^+]_o$ (in green) when the cell's voltage was held at -142 mV. $n = 11$ and 10 cells for 2.5 and 50 mM $[K^+]_o$ group, respectively. The error bars represent SEM. *** indicates $p < .001$, two-tailed unpaired *T*-test

FIGURE 6 (a) Representative traces show macroscopic K^+ currents (in black) after bath application of the Kir6.1 channel inhibitor glibenclamide (10 μM) (in red) and glibenclamide-sensitive Kir6.1 currents (in gray) under 15 mM $[K^+]_o$ in a whole-cell patched pericyte in NG2-DsRed transgenic mouse hippocampus. (b) Representative traces show macroscopic K^+ currents (in black), macroscopic currents after bath application of the Kir4.1 channel antagonist VU0134992 (15 μM) (in red) and VU-sensitive Kir4.1 currents (in purple) under 15 mM $[K^+]_o$ in a whole-cell patched pericyte in NG2-DsRed transgenic mouse hippocampus. (c) Left panel shows the average I/V plot of the Kir6.1 channel-mediated currents and Kir4.1 channel-mediated currents under 15 mM $[K^+]_o$. Right panel shows the bar graph summary of the Kir6.1 current and Kir4.1 current when the cell's voltage was held at -142 mV under 15 mM $[K^+]_o$. $n = 6$ for each group. The error bars represent SEM. ** indicates $p < .01$, two-tailed unpaired T-test. (d) Upper panel shows the experimental diagram of the approach for recording inward K^+ channel currents of pericytes in hypoxia. The lower panel shows two representative traces of inward K^+ currents of a recorded pericyte in control condition (in black) and in hypoxic condition (in red). The red arrow indicates the augmentation of K^+ currents in pericyte induced by hypoxia. (e) Bar graph summary shows the inward K^+ currents in hypoxia relative to the control with the holding voltage at -142 mV, $n = 7$ cells. The error bars represent SEM. ** indicates $p < .01$, two-tailed paired T-test

Astrocytes, as a major component of the glial cell population, are well known to contribute to the spatial K^+ buffering around neurons due to their high expression of Kir4.1 channels (Nwaobi et al., 2016; Olsen & Sontheimer, 2008; Tong et al., 2014; Tong et al., 2013; Zhang et al., 2018). Meanwhile, astrocytes also are one of the most important components of the NVU by making extensive contacts with blood vessels in the CNS. We therefore examined whether high concentration of external K^+ has an effect on Ba^{2+}-sensitive Kir4.1 channel currents in astrocytes as well. Consistent with the previous reports, GFAP-labeled astrocytes in 2.5 mM $[K^+]_o$ showed hyperpolarized RMPs and low membrane input resistances (the average of RMP was: -96 ± 0.67 mV; the average of Rm was: 17.51 ± 1.12 MΩ, $n = 10$ cells, Figure 5a,b) (Shigetomi et al., 2013; Song et al., 2018; Tong et al., 2014). Interestingly, we did not find a significant increase of Kir4.1 currents in astrocytes by changing the $[K^+]_o$ from 2.5 to 50 mM when the cell's voltage was held at -142 mV (-955.07 ± 183.48 pA for basal v.s -1218.33 ± 293.68 pA for 50 mM $[K^+]_o$, $n = 11$ and 10 cells for basal and 50 mM $[K^+]_o$ group, respectively. $p > .05$, two-tailed unpaired T-test, Figure 5c–g). Moreover, the percentage of Ba^{2+}-sensitive Kir4.1 currents from the total K^+ macroscopic currents declined to 13% due to the augmentation of total macroscopic currents in 50 mM $[K^+]_o$ when the cell's voltage was held at -142 mV ($33.04\% \pm 3.82$ for basal v.s $12.52\% \pm 2.49$ for 50 mM $[K^+]_o$, $n = 11$ and 10 cells for basal and 50 mM $[K^+]_o$ group, respectively. $p < .001$, two-tailed unpaired T-test, Figure 5h). Taken together, in physiological $[K^+]_o$ levels, astrocytes are more responsive to Kir4.1 inhibition. When $[K^+]_o$ is elevated to pathological levels such as 15 or 50 mM, pericytes Kir4.1 channels exhibit heightened sensitivity and are robustly activated, indicating a K^+ homeostatic regulation in local neural networks by both astrocytes and pericytes during physiological and pathological conditions.

3.5 | Kir4.1 but not Kir6.1 in pericytes is crucial to the elevation of extracellular potassium and plays a role in hypoxia

As previously described, the RNA-seq data indicates that Kir6.1-encoding gene *Kcnj8* is expressed at a higher level than *Kcnj10* (Figure 3b). Kir6.1 is a component of ATP sensitive potassium channels (K_{ATP}) and this channel is only activated when the cellular ATP levels fall. Kir6.1 channels play a variety of physiological roles including controlling the release of insulin from pancreatic β cells and regulating blood vessel tone and blood pressure (Tinker et al., 2018). To further determine whether the increase of external K^+ could induce Kir6.1-mediated currents in pericytes, we used Kir6.1 channel specific blocker glibenclamide to detect the Kir6.1 channel currents under 15 mM $[K^+]_o$ (Wang et al., 2003). As shown in Figure 6a,c, glibenclamide at 10 μM did not inhibit the augmented K^+ currents in pericytes when extracellular K^+ was set at 15 mM (glibenclamide-sensitive Kir6.1 currents were -9.29 ± 4.80 pA at the holding voltage of -142 mV, $n = 6$ cells). In contrast, a newly reported Kir4.1 specific antagonist selected by Tl^+ flux assay (Kharade et al., 2018),

VU0134992 at 15 μM exhibited a similar blockade effect as 100 μM Ba^{2+} on the augmented K^+ currents in pericytes under 15 mM K^+ (VU-sensitive Kir4.1 currents was -87.67 ± 7.81 pA, $n = 6$ cells, $p < .01$ compared with glibenclamide-sensitive Kir6.1 currents, two-tailed unpaired T-test, Figure 6b,c), suggesting that Kir4.1 but not Kir6.1 in pericytes is more sensitive to an elevation of extracellular K^+.

It has been reported that under pathological conditions such as stroke and hypoxia, the local $[K^+]_o$ can rise substantially, up to 12–70 mM (Chao et al., 2007; Milton & Smith, 2018; Syková et al., 1994). Therefore, to further investigate whether pericyte Kir4.1 plays a role in such pathological condition, we compared the change of inward K^+ currents of an individual patch clamp-recorded pericyte before and after the cell underwent an acute hypoxic condition. As shown in Figure 6d,e, we found a $29\% \pm 3.1$ increase of the inward K^+ currents in pericytes after the cells were exposed to acute hypoxia (the inward K^+ currents in hypoxia: $129\% \pm 3.1$ relative to its control: $100\% \pm 7.10$ when the cells were held at the voltage of -142 mV, $p < .01$, two-tailed paired T-test, $n = 7$ cells). Taken together, Kir4.1 channels in pericytes demonstrate an exquisite sensitivity to elevations of external K^+ especially in pathological conditions and hypoxia, indicating a role in the regulation of K^+ homeostasis in the local neurovascular networks under such circumstances.

4 | DISCUSSION

It is well accepted that vascular pericytes are heterogeneous and can be divided into three main subtypes, ensheathing, mesh and thin-strand pericytes in terms of their distinct morphology, location and specific protein expression (Attwell et al., 2016; Gonzales & Klug, 2020; Grant et al., 2019). However, in our present study, by utilizing electrophysiological recordings of the three subtypes of pericytes in situ and RNA sequencing transcriptomic analysis, we found: (1) There is no significant difference of intrinsic membrane properties between the three subtypes of pericytes in the CNS. (2) Transcriptomic analysis revealed that Kir4.1 ion channels homogeneously express in brain pericytes. (3) Systematic electrophysiological analysis illustrated that pericytes Kir4.1 channels play a crucial role as local K^+ sensors and help maintain K^+ homeostasis in the local neurovascular networks.

Brain pericytes are normally embedded within the vascular basement membrane, which makes it difficult to obtain successful whole-cell patch-clamp recordings in acute brain slices in situ. In addition, pericytes easily slide away from the patch electrode during whole-cell patch-clamp recordings due to vascular elasticity. Thus, the past electrophysiological recordings of single pericytes from the cochlear stria vascularis or retina were limited to dissociated pericytes in vitro (Cao et al., 2006; Liu et al., 2018; Matsushita & Puro, 2006). The average cell membrane potential of pericytes in the stria vascularis is -30.9 mV without clearly identified subtype of pericyte (Liu et al., 2018). In our study, we utilized an improved patch-clamp method by digesting the brain slices with papain for 10 min first to

dissociate the vascular basement membrane yet to keep the vascular structure intact. This fine electrophysiological technique can not only dissociate the wrapped fascia from the patched pericyte, but also keep an anatomical structure of the brain slice so as to easily identify the subtype of a patched cell in situ. Our electrophysiological results showed that the average RMP of the three types of pericytes is close to -60 mV, which is much hyperpolarized than previously published data and thus indicates a more physiological environment surrounding the pericytes that we recorded.

Kir4.1 channel is another component of the neurovascular coupling and has been well studied in astrocytes. In astroglia, Kir4.1 channels contribute to high resting K^+ conductance and hyperpolarized RMP (Nwaobi et al., 2016; Olsen & Sontheimer, 2008; Tong et al., 2014; Tong et al., 2013; Zhang et al., 2018). However, it remained largely unknown whether pericytes express Kir4.1 channels and which subtype of potassium channel contributes to the intrinsic membrane properties of pericytes. By using RNA-seq transcriptomic analysis, we unexpectedly found that *Kcnj10* gene expresses in isolated pericytes in adult mouse brain. Electrophysiological studies further demonstrated that *Kcnj10*-coded Kir4.1 channel currents could be functionally induced in hippocampal pericytes. Interestingly, when compared with the RMPs ($\sim$96 mV) in astrocytes (Figure 5b), pericytes exhibited more depolarized RMPs ($\sim$60 mV) (Figure 2b) when the $[K^+]_o$ was set at 2.5 mM. A much smaller Ba^{2+}-sensitive Kir4.1 current ($\sim$1.1% of total macroscopic K^+ currents) could be the main explanation for the depolarized RMP in pericytes as those channels are mostly closed in a physiological state. In contrast, when extracellular K^+ was increased to 15 and 50 mM, Ba^{2+}- or VU-sensitive Kir4.1 currents in pericytes were significantly augmented (Figures 4c–h and 6b,c), indicating that pericytes Kir4.1 channels opened rapidly in high potassium levels and the augmentation of Kir4.1 channel currents exhibited a dose-dependent increase upon the changes in the external K^+ concentration. Although we did not find any significant change of Ba^{2+}-sensitive Kir4.1 channel currents in astrocytes when the $[K^+]_o$ was increased to a high level of 50 mM (Figure 5c–g), it has been reported that astrocytic Kir4.1 could act as a temporal $[K^+]_o$ sink when a rapid accumulation of $[K^+]_o$ occurs during neuronal activity in physiological conditions (Larsen et al., 2016). Thus, it suggests that pericyte Kir4.1 channels are robustly activated at pathological K^+ levels while astrocytes might be more responsive to Kir4.1 inhibition at lower K^+ levels.

Previous studies have shown that pericytes express both Kir6.1 and inward rectifier subunits sulfonylurea receptor subtype 2B by immunostaining and in situ hybridization (Bondjers et al., 2006). Kir6.1 belongs to K_{ATP} channel. The biophysical feature of K_{ATP} channels is that the open probability (P_o) decreases with increments of intracellular ATP levels by stabilizing the closed state of the channel. When cellular ATP demands are low and free cytosolic ATP is high, Kir6.1 channel is closed. In contrast, when cell activity increases or metabolism drops, the Kir6.1 channel may open to hyperpolarize the membrane (Hibino et al., 2010). Thus, Kir6.1 channels may act as sensors of the metabolic state of the cell as an elevation of external K^+ does not activate those channels in pericytes (Figure 6a). Notably, external K^+ is also an important mediator of neurovascular coupling as well as ATP. Recently, Gonzales et al. reported that pericytes at the first two

to three capillary junctions proximal to the feeding artery rapidly contracted following administration of 60 mM KCl, and was accompanied by an enhancement of Ca^{2+} signals (Gonzales & Klug, 2020). Inwardly rectifying K^+ channels can be activated by external K^+. Opening of Kir channels leads to a net depolarization of pericytes due to a large increase in $[K^+]_o$ to the level whereby E_K exceeds (more positive than) E_{rest}. Therefore, it is important to further investigate whether Kir4.1 channels mediate the excitability of the pericytes and subsequent arterial contraction. In addition, pericyte constriction is commonly observed in pathological conditions such as stroke and hypoxia, where the local $[K^+]_o$ can rise substantially higher to 12–70 mM (Chao et al., 2007; Milton & Smith, 2018; Syková et al., 1994). Indeed, in an acute hypoxic condition, our data suggest a 29% increase of inward K^+ currents occurred in pericytes, which exactly mimics 15 mM external K^+-induced Kir4.1 channel currents in pericytes (Figure 6d,e). In conclusion, Kir4.1 channels in pericytes provide a therapeutic target for the treatment of neurovascular diseases, based on their exquisite capacity to sense local high K^+ levels required for maintaining K^+ homeostasis in local neurovascular networks.

CONFLICT OF INTEREST

The authors declare no competing interests.

AUTHOR CONTRIBUTIONS

Huimin Zhang and Xiao Zhang were responsible for conducting electrophysiology, immunohistochemistry and data analysis. Xiaoqi Hong, Xiao Zhang and Huimin Zhang carried out RNA-sequencing, single-cell RT-PCR and data analysis. Xiaoping Tong directed the work and wrote the article. All of the authors contributed to the final version of the manuscript.

DATA AVAILABILITY STATEMENT

The authors declare that all data supporting the findings of this study are available within the article and its supplementary information files. All relevant data not present within the manuscript or supplementary files are available from the corresponding author upon reasonable request. RNA-sequencing data are deposited at the Sequence Read Archive with SRA accession number PRJNA695351.

ORCID

Xiao Zhang https://orcid.org/0000-0003-1622-9937
Xiaoping Tong https://orcid.org/0000-0002-0908-8091

REFERENCES

Attwell, D., Mishra, A., Hall, C. N., O'Farrell, F. M., & Dalkara, T. (2016). What is a pericyte? *Journal of Cerebral Blood Flow & Metabolism*, *36*(2), 451–455. https://doi.org/10.1177/0271678x15610340

Berthiaume, A. A., Hartmann, D. A., Majesky, M. W., Bhat, N. R., & Shih, A. Y. (2018). Pericyte structural remodeling in cerebrovascular health and homeostasis. *Frontiers in Aging Neuroscience*, *10*, 210. https://doi.org/10.3389/fnagi.2018.00210

Birbrair, A. (2018). Pericyte biology: Development, homeostasis, and disease. *Advances in Experimental Medicine and Biology*, *1109*, 1–3. https://doi.org/10.1007/978-3-030-02601-1_1

Bondjers, C., He, L., Takemoto, M., Norlin, J., Asker, N., Hellström, M., ... Betsholtz, C. (2006). Microarray analysis of blood microvessels from PDGF-B and PDGF-Rbeta mutant mice identifies novel markers for brain pericytes. *Federation of American Societies for Experimental Biology Journal*, *20*(10), 1703–1705. https://doi.org/10.1096/fj.05-4944fje

Cao, C., Goo, J. H., Lee-Kwon, W., & Pallone, T. L. (2006). Vasa recta pericytes express a strong inward rectifier K^+ conductance. *American Journal of Physiology, Regulatory, Integrative and Comparative Physiology*, *290*(6), R1601–R1607. https://doi.org/10.1152/ajpregu.00877.2005

Chao, D., Bazzy-Asaad, A., Balboni, G., & Xia, Y. (2007). Delta-, but not mu-, opioid receptor stabilizes $K^{(+)}$ homeostasis by reducing $Ca^{(2+)}$ influx in the cortex during acute hypoxia. *Journal of Cellular Physiology*, *212*(1), 60–67. https://doi.org/10.1002/jcp.21000

Cheng, J., Korte, N., Nortley, R., Sethi, H., Tang, Y., & Attwell, D. (2018). Targeting pericytes for therapeutic approaches to neurological disorders. *Acta Neuropathologica*, *136*(4), 507–523. https://doi.org/10.1007/s00401-018-1893-0

Cui, Y., Yang, Y., Ni, Z., Dong, Y., Cai, G., Foncelle, A., ... Hu, H. (2018). Astroglial Kir4.1 in the lateral habenula drives neuronal bursts in depression. *Nature*, *554*(7692), 323–327. https://doi.org/10.1038/nature25752

Giannoni, P., Badaut, J., Dargazanli, C., De Maudave, A. F., Klement, W., Costalat, V., & Marchi, N. (2018). The pericyte-glia interface at the blood-brain barrier. *Clinical Science*, *132*(3), 361–374. https://doi.org/10.1042/cs20171634

Gonzales, A. L., & Klug, N. R. (2020). Contractile pericytes determine the direction of blood flow at capillary junctions. *Proceedings of the National Academy of Sciences of the United States of America*, *117*(43), 27022–27033. https://doi.org/10.1073/pnas.1922755117

Grant, R. I., Hartmann, D. A., Underly, R. G., Berthiaume, A. A., Bhat, N. R., & Shih, A. Y. (2019). Organizational hierarchy and structural diversity of microvascular pericytes in adult mouse cortex. *Journal of Cerebral Blood Flow and Metabolism: Official Journal of the International Society of Cerebral Blood Flow and Metabolism*, *39*(3), 411–425. https://doi.org/10.1177/0271678x17732229

Hall, C. N., Reynell, C., Gesslein, B., Hamilton, N. B., Mishra, A., Sutherland, B. A., ... Attwell, D. (2014). Capillary pericytes regulate cerebral blood flow in health and disease. *Nature*, *508*(7494), 55–60. https://doi.org/10.1038/nature13165

Hibino, H., Inanobe, A., Furutani, K., Murakami, S., Findlay, I., & Kurachi, Y. (2010). Inwardly rectifying potassium channels: Their structure, function, and physiological roles. *Physiological Reviews*, *90*(1), 291–366. https://doi.org/10.1152/physrev.00021.2009

Kharade, S. V., Kurata, H., Bender, A. M., Blobaum, A. L., Figueroa, E. E., Duran, A., ... Denton, J. S. (2018). Discovery, characterization, and effects on renal fluid and electrolyte excretion of the Kir4.1 potassium channel pore blocker, VU0134992. *Molecular Pharmacology*, *94*(2), 926–937. https://doi.org/10.1124/mol.118.112359

Kornfield, T. E., & Newman, E. A. (2014). Regulation of blood flow in the retinal trilaminar vascular network. *The Journal of Neuroscience*, *34*(34), 11504–11513. https://doi.org/10.1523/jneurosci.1971-14.2014

Larsen, B. R., Stoica, A., & MacAulay, N. (2016). Managing brain extracellular $K^{(+)}$ during neuronal activity: The physiological role of the $Na^{(+)}/K^{(+)}$-ATPase subunit isoforms. *Frontiers in Physiology*, *7*, 141. https://doi.org/10.3389/fphys.2016.00141

Li, C. L., Li, K. C., Wu, D., Chen, Y., Luo, H., Zhao, J. R., ... Hu, X. Y. (2016). Somatosensory neuron types identified by high-coverage single-cell RNA-sequencing and functional heterogeneity. *Cell Research*, *26*(8), 967. https://doi.org/10.1038/cr.2016.90

Liu, Y. H., Zhang, Z. P., Wang, Y., Song, J., Ma, K. T., Si, J. Q., & Li, L. (2018). Electrophysiological properties of strial pericytes and the effect of aspirin on pericyte K^+ channels. *Molecular Medicine Reports*, *17*(2), 2861–2868. https://doi.org/10.3892/mmr.2017.8194

Longden, T. A., Dabertrand, F., Koide, M., Gonzales, A. L., Tykocki, N. R., Brayden, J. E., ... Nelson, M. T. (2017). Capillary $K^{(+)}$-sensing initiates retrograde hyperpolarization to increase local cerebral blood flow. *Nature Neuroscience*, *20*(5), 717–726. https://doi.org/10.1038/nn.4533

Longden, T. A., & Nelson, M. T. (2015). Vascular inward rectifier K^+ channels as external K^+ sensors in the control of cerebral blood flow. *Microcirculation (New York, NY: 1994)*, *22*(3), 183–196. https://doi.org/10.1111/micc.12190

Matsushita, K., & Puro, D. G. (2006). Topographical heterogeneity of K(IR) currents in pericyte-containing microvessels of the rat retina: Effect of diabetes. *The Journal of Physiology*, *573*(Pt 2), 483–495. https://doi.org/10.1113/jphysiol.2006.107102

Milton, M., & Smith, P. D. (2018). It's all about timing: The involvement of Kir4.1 channel regulation in acute ischemic stroke pathology. *Frontiers in Cellular Neuroscience*, *12*, 36. https://doi.org/10.3389/fncel.2018.00036

Moody, W. J., Futamachi, K. J., & Prince, D. A. (1974). Extracellular potassium activity during epileptogenesis. *Experimental Neurology*, *42*(2), 248–263. https://doi.org/10.1016/0014-4886(74)90023-5

Nwaobi, S. E., Cuddapah, V. A., Patterson, K. C., Randolph, A. C., & Olsen, M. L. (2016). The role of glial-specific Kir4.1 in normal and pathological states of the CNS. *Acta Neuropathologica*, *132*(1), 1–21. https://doi.org/10.1007/s00401-016-1553-1

Olsen, M. L., & Sontheimer, H. (2008). Functional implications for Kir4.1 channels in glial biology: From K^+ buffering to cell differentiation. *Journal of Neurochemistry*, *107*(3), 589–601. https://doi.org/10.1111/j.1471-4159.2008.05615.x

Picelli, S., Faridani, O. R., Björklund, A. K., Winberg, G., Sagasser, S., & Sandberg, R. (2014). Full-length RNA-seq from single cells using smart-seq2. *Nature Protocols*, *9*(1), 171–181. https://doi.org/10.1038/nprot.2014.006

Shankar, R., & Quastel, J. H. (1972). Effects of tetrodotoxin and anaesthetics on brain metabolism and transport during anoxia. *The Biochemical Journal*, *126*(4), 851–867. https://doi.org/10.1042/bj1260851

Shigetomi, E., Bushong, E. A., Haustein, M. D., Tong, X., Jackson-Weaver, O., Kracun, S., ... Khakh, B. S. (2013). Imaging calcium microdomains within entire astrocyte territories and endfeet with GCaMPs expressed using adeno-associated viruses. *The Journal of General Physiology*, *141*(5), 633–647. https://doi.org/10.1085/jgp.201210949

Song, F., Hong, X., Cao, J., Ma, G., Han, Y., Cepeda, C., & Kang, Z. (2018). Kir4.1 channels in NG2-glia play a role in development, potassium signaling, and ischemia-related myelin loss. *Communications Biology*, *1*, 80. https://doi.org/10.1038/s42003-018-0083-x

Sonkusare, S. K., Dalsgaard, T., Bonev, A. D., & Nelson, M. T. (2016). Inward rectifier potassium (Kir2.1) channels as end-stage boosters of endothelium-dependent vasodilators. *The Journal of Physiology*, *594*(12), 3271–3285. https://doi.org/10.1113/jp271652

Syková, E., Svoboda, J., Polák, J., & Chvátal, A. (1994). Extracellular volume fraction and diffusion characteristics during progressive ischemia and terminal anoxia in the spinal cord of the rat. *Journal of Cerebral Blood Flow and Metabolism: Official Journal of the International Society of Cerebral Blood Flow and Metabolism*, *14*(2), 301–311. https://doi.org/10.1038/jcbfm.1994.37

Tinker, A., Aziz, Q., Li, Y., & Specterman, M. (2018). ATP-sensitive potassium channels and their physiological and pathophysiological roles.

Comprehensive Physiology, 8(4), 1463–1511. https://doi.org/10.1002/cphy.c170048

Toledo-Rodriguez, M., & Markram, H. (2014). Single-cell RT-PCR, a technique to decipher the electrical, anatomical, and genetic determinants of neuronal diversity. *Methods in Molecular Biology (Clifton, NJ)*, 1183, 143–158. https://doi.org/10.1007/978-1-4939-1096-0_8

Tong, X., Ao, Y., Faas, G. C., Nwaobi, S. E., Xu, J., Haustein, M. D., ... Khakh, B. S. (2014). Astrocyte Kir4.1 ion channel deficits contribute to neuronal dysfunction in Huntington's disease model mice. *Nature Neuroscience*, 17(5), 694–703. https://doi.org/10.1038/nn.3691

Tong, X., Shigetomi, E., Looger, L. L., & Khakh, B. S. (2013). Genetically encoded calcium indicators and astrocyte calcium microdomains. *The Neuroscientist: A Review Journal Bringing Neurobiology, Neurology and Psychiatry*, 19(3), 274–291. https://doi.org/10.1177/1073858412468794

Verkhratsky, A., Augusto-Oliveira, M., Pivoriūnas, A., Popov, A., Brazhe, A., & Semyanov, A. (2021). Astroglial asthenia and loss of function, rather than reactivity, contribute to the ageing of the brain. *Pflügers Archiv: European Journal of Physiology*, 473(5), 753–774. https://doi.org/10.1007/s00424-020-02465-3

Wang, X., Wu, J., Li, L., Chen, F., Wang, R., & Jiang, C. (2003). Hypercapnic acidosis activates KATP channels in vascular smooth muscles. *Circulation Research*, 92(11), 1225–1232. https://doi.org/10.1161/01.res.0000075601.95738.6d

Zhang, X., Wan, J. Q., & Tong, X. P. (2018). Potassium channel dysfunction in neurons and astrocytes in Huntington's disease. *CNS Neuroscience & Therapeutics*, 24(4), 311–318. https://doi.org/10.1111/cns.12804

Zhang, Y., Sloan, S. A., Clarke, L. E., Caneda, C., Plaza, C. A., Blumenthal, P. D., ... Duncan, J. A., III. (2016). Purification and characterization of progenitor and mature human astrocytes reveals transcriptional and functional differences with mouse. *Neuron*, 89(1), 37–53. https://doi.org/10.1016/j.neuron.2015.11.013

Zhao, H., Darden, J., & Chappell, J. C. (2018). Establishment and characterization of an embryonic pericyte cell line. *Microcirculation (New York, NY: 1994)*, 25(5), e12461. https://doi.org/10.1111/micc.12461

Zhu, X., Hill, R. A., & Nishiyama, A. (2008). NG2 cells generate oligodendrocytes and gray matter astrocytes in the spinal cord. *Neuron Glia Biology*, 4(1), 19–26. https://doi.org/10.1017/s1740925x09000015